INTERNATIONAL JOURNAL FOR NUMERICAL METHODS IN FLUIDS
Int. J. Numer. Meth. Fluids 2002; **40**:1019–1030 (DOI: 10.1002/fld.388)

An operator-splitting finite-element approach to the 8:1 thermal-cavity problem

D. Davis*,† and E. Bänsch

Weierstrass Institute for Applied Analysis and Stochastics, Mohrenstrasse 39, D-10117 Berlin, Germany

SUMMARY

This article describes the methodology for, and results obtained from, our contribution to the thermal-cavity benchmark test. Our solutions were obtained on graded rectangular grids for two different time-discretization schemes by applying a finite-element procedure to the model equations, and a combination of conjugate-gradient and GMRES solvers to the resulting matrix systems. Copyright © 2002 John Wiley & Sons, Ltd.

KEY WORDS: finite element; advection; Navier–Stokes; CG method; GMRES; Galerkin

INTRODUCTION

In the following we describe our contribution to a thermal-cavity benchmark problem held at the First MIT Conference on Computational Fluid and Solid Mechanics 2001; a fully detailed account of the problem can be found in Reference [1]. To discretize the governing equations in time, an operator-splitting, multiple-step integrator was applied to the Navier–Stokes part, while the energy equation was treated using one of two methods: a (first-order) backward-Euler-type scheme and a Crank–Nicolson-type scheme, both with semi-implicit advective part. For the spatial approximation, a standard Galerkin method was implemented, with the discrete velocity and temperature spaces being defined by piecewise bi-quadratic, globally continuous basis functions and the discrete pressure space by piecewise bi-linear, globally continuous basis functions. Hence, the Taylor–Hood $Q_2 - Q_1$ element is used. Zero initial conditions were adopted in all of our computations. Results were obtained for both time integrators on grids comprising: (i) 11×51, (ii) 21×101 or (iii) 41×201 elements; the grids were furthermore graded near the vertical and horizontal walls of the cavity, owing to the presence of very large temperature boundary layers there, notably during the initial transient phase.

* Correspondence to: D. Davis, Weierstrass Institute for Applied Analysis and Stochastics, Mohrenstrasse 39, D-10117 Berlin, Germany.
† E-mail: davis@wias-berlin.de

Received 31 December 2001
Revised 1 July 2002

NUMERICAL APPROXIMATION

Temporal discretization

In order to meet the demands of efficiency and accuracy, and avoid problems caused by numerical damping and/or over-smoothing, the time-discretization procedure for the governing system requires judicious selection.

Concerning the Navier–Stokes part first, we felt it important here, given the nature of the flow problem (i.e. advection-dominated), to choose an appropriate method of time discretization which could be both A-stable and virtually non-dissipative, as well as being inherently accurate (preferably, second order).

The fractional θ-scheme with operator-splitting as variant [2, 3] seemed therefore a suitable option, and in addition led to a favourable decoupling of the incompressibility constraint and the non-linearity, as outlined below.

The underlying mechanism of this procedure can perhaps best be observed by considering the following N-dimensional, first-order equation:

$$\frac{\mathrm{d}\mathbf{q}}{\mathrm{d}t} + A\mathbf{q} = \mathbf{0} \quad \text{for } t > 0$$

with initial condition

$$\mathbf{q}(0) = \mathbf{q}_0$$

where A is a known $N \times N$ matrix, $\mathbf{q}_0$ is a known N-vector, and, for $t > 0$, $\mathbf{q}(t)$ is an unknown N-vector to be determined. To apply this method, we first break the integration step into three smaller sub-steps $[t_n, t_n + \theta\tau_n]$, $[t_n + \theta\tau_n, t_n + (1-\theta)\tau_n]$ and $[t_n + (1-\theta)\tau_n, t_{n+1}]$ with $\tau_n := t_{n+1} - t_n$ denoting the total time step, and $\theta \in (0, 0.5)$ an arbitrary parameter. Then, for each interval, we 'split' the matrix–vector term into an implicit and an explicit part, with each part a non-trivial linear multiple of the original term evaluated at the 'current' and 'previous' time, respectively; this is performed in the following manner:

$$\frac{\mathbf{q}^{n+\theta} - \mathbf{q}^{n}}{\theta\tau_n} + \alpha A\mathbf{q}^{n+\theta} + (1-\alpha)A\mathbf{q}^{n} = \mathbf{0}$$

$$\frac{\mathbf{q}^{n+1-\theta} - \mathbf{q}^{n+\theta}}{(1-2\theta)\tau_n} + \alpha A\mathbf{q}^{n+\theta} + (1-\alpha)A\mathbf{q}^{n+1-\theta} = \mathbf{0}$$

$$\frac{\mathbf{q}^{n+1} - \mathbf{q}^{n+1-\theta}}{\theta\tau_n} + \alpha A\mathbf{q}^{n+1} + (1-\alpha)A\mathbf{q}^{n+1-\theta} = \mathbf{0}$$

where $\alpha \in (\frac{1}{2}, 1)$ is the single parameter controlling the splitting of the matrix–vector term.

With the choice $\theta = 1 - \sqrt{2}/2 (\approx 0.293)$, we obtain a second-order accurate method, which for *positive-definite* matrices A is unconditionally stable. Furthermore, choosing $\alpha = (1-2\theta)/(1-\theta) (\approx 0.586)$, ensures identical implicit operators for each of the three sub-intervals, which eases computation.

Another important advantage of the fractional θ-scheme is that eigenmodes are *uniformly* damped, allowing steady-state flows (or 'near-steady-state flows', as is relevant here) to be more reliably calculated.

In Reference [2], the fractional θ-scheme was applied with operator splitting as variant to the Navier–Stokes equations in the following manner: with the above-described splitting applied to the diffusion operator, the non-linear convection term is treated as full explicit in the first and third steps, but full implicit in the second step; these rôles are exactly reversed for the pressure gradient, while the incompressibility constraint is relaxed in the second step. The general upshot of this form of discretization is to produce two distinct types of sub-problem: (i) a self-adjoint, quasi-linear, Stokes system for unknown velocity and pressure and (ii) an asymmetric, non-linear system for velocity only.

Finally, the thermal source terms are approximated using the (explicit) temperature value at time t_n, for each of the three steps. This simple approximation generally leads to the above scheme being only first-order accurate, but we apply this nonetheless, since the *overall* system (due to the 'first-order accuracy only' of the two types of energy-equation time discretizations considered—described next) is forced to have this degree of accuracy anyway.

To assess and compare the effectiveness of different forms of time discretization for the energy equation, we considered two possibilities based on a first-order backward–Euler scheme and a second-order Crank–Nicolson scheme.

For both cases, the advection term is treated semi-implicitly using the previous velocity value ($\mathbf{u}^n$), while the temperature part, as for the remaining terms in the energy equation, are discretized according to the backward–Euler and Crank–Nicolson schemes. Although simple to implement and naturally stable (unconditionally, moreover), the backward–Euler-type scheme (hereafter referred to as BE) suffers from numerical dissipation, as well as being only first-order accurate—hence, not ideally suited to the nature of the problem in hand (as reflected to a certain extent in the results below); the Crank–Nicolson-type scheme (CN) is also of first-order accuracy, owing to the (first-order) velocity coupling, but an important distinction to BE is the inherent property of non-dissipation associated with Crank–Nicolson-type schemes.

We note that both schemes lead to asymmetric systems, whose solution procedure is described below.

Finite-element discretization

For the spatial discretization of the model equations, a standard Bubnov–Galerkin finite-element method was applied using continuous, piecewise bi-quadratic basis functions for the discrete velocity and temperature spaces ($:= V_h$), and continuous, piecewise bi-linear basis functions for the discrete pressure space ($:= W_h$), i.e. the Taylor–Hood quadrilateral element, $Q_2 - Q_1$. This element, fulfilling the requirements of the inf–sup (LBB) stability constraint, avoids any possible complications with spurious pressure modes, and, as well as being relatively straightforward to implement, gives a good balance between efficiency of computation and accuracy. For this element, the velocity and temperature are of second-order spatial accuracy when measured relative to the $H^1(\Omega)$ norm, while pressure has the same degree of spatial accuracy when measured relative to the $L^2(\Omega)$ norm.

Solution procedure

Here we recapitulate the main aspects of the numerical solution procedure, in the order of application:

(a) Specify $\mathbf{u}_0$, T_0. (Both are zero-valued here.)
For $n \geqslant 0$:

(b) Solve the energy equation for $t_n \rightarrow t_{n+1}$.
(c) Solve the Navier–Stokes equations with incompressibility constraint for:
  (i) $t_n \rightarrow t_{n+\theta}$,
  (ii) $t_{n+\theta} \rightarrow t_{n+1-\theta}$,
  (iii) $t_{n+1-\theta} \rightarrow t_{n+1}$.
(d) Repeat (b), (c) until end-time $= t_E$.

ALGEBRAIC SUB-PROBLEMS

Quasi-steady Stokes system

As described in the previous section, the application of the fractional θ-scheme to the Navier–Stokes part of our model equations renders a linear, self-adjoint system for the first and third sub-steps, these resembling the steady Stokes equations. After full (time and space) discretization, we need to solve a matrix system of the form

$$\begin{pmatrix} A(\gamma_n) & B \\ B^T & 0 \end{pmatrix} \begin{pmatrix} u_h^c \\ p_h^c \end{pmatrix} = \begin{pmatrix} f_h^c \\ 0 \end{pmatrix}$$

Here $A(\gamma_n)$ is the symmetric positive-definite (SPD) stiffness matrix for the discrete velocity $\mathbf{u}_h = (u_h, v_h)$ whose corresponding co-ordinate vector (with respect to the given basis functions of the discrete velocity space, V_h) is $u_h^c = [u_h^1, \ldots, u_h^{N_v} \mid v_h^1, \ldots, v_h^{N_v}]$, with N_v denoting the dimension of V_h, i.e. the number of velocity 'nodes'. The matrix A depends on the discretization parameter $\gamma_n := \theta\tau_n\alpha\sqrt{Pr/Ra}$, which we note is small in the problem under observation, (e.g. $\gamma_n = 2.48 \times 10^{-5}$ for a time step as large as 0.1). Also here we have the discrete gradient matrix B, its transpose (which represents discrete divergence), and the pressure vector, which has an analogous definition to that for velocity, i.e. $p_h^c = [p_h^1, \ldots, p_h^{N_p}]$, with N_p the number of pressure 'nodes'. Finally, f_h^c denotes the co-ordinate vector of the discrete momentum source term f_h. For brevity, we have dispensed with time step superscripts on the vector quantities.

Since A is invertible, we can form the Schur complement equation for the pressure vector as follows:

$$C(\gamma_n)\, p_h^c := (B^T A^{-1}(\gamma_n) B)\, p_h^c = B^T A^{-1} f_h^c$$

Moreover, since B has full rank and, owing to the relatively small pressure space ($\dim W_h < \dim V_h$) for the Taylor–Hood element, has more rows than columns, it follows that C is SPD for any given (positive) γ_n. Unfortunately, however, its condition number explodes as $\gamma_n \rightarrow 0^+$, precluding the possibility of applying a suitable minimization solver, such as the method of conjugate gradients (CG method). To circumvent the problem of large condition number, we apply a special type of preconditioner, as first proposed in Reference [2].

Asymmetric advection system

This system, which arises from the spatially discretized form of the second step of the fractional θ-scheme for the Navier–Stokes equations, as well as from the full discretization of

the energy equation, has the general form

$$Mx_h^c = g_h^c$$

where M is an *asymmetric* $2N_v \times 2N_v$ (or $N_v \times N_v$, as appropriate) stiffness matrix for the coefficient vector $x_h^c = [u_h^1, \ldots, u_h^{N_v} | v_h^1, \ldots, v_h^{N_v}]$ (or $[T_h^1, \ldots, T_h^{N_v}]$), and g_h^c the source term. Furthermore, we note that M is variable dependent, in the former case. To solve this matrix system, we applied the GMRES solver [4] using a Krylov subspace dimension of 15. In addition, for the velocity solver, the 'current' velocity value was periodically used to update the matrix M.

GRID GENERATION

Following the guidelines suggested in the Special Session Document [1], we selected grids aligned with the co-ordinate directions and composed of E_x elements in the x-direction and E_y elements in the y-direction, with $E_x : E_y \approx 1{:}5$ ($\rightarrow 1{:}5$, as $E_x, E_y \rightarrow \infty$). Specifically, we ran our computations on three different grids with increasing refinement: 11×51 elements ('coarse'), 21×101 elements ('medium') and 41×201 elements ('fine').

Owing to the rapid flow-variable changes near the walls, in particular the presence of strong thermal boundary layers on the vertical walls, the grid required appropriate grading in these regions. For this purpose, we defined the following functions:

$$h_1(j) = \left(\frac{\hat{h}_1(j)}{\sum_{j_1=1}^{E_x} \hat{h}_1(j_1)} \right) W \quad \text{for } j = 1, \ldots, E_x$$

$$h_2(k) = \left(\frac{\hat{h}_2(k)}{\sum_{k_1=1}^{E_y} \hat{h}_2(k_1)} \right) H \quad \text{for } k = 1, \ldots, E_y$$

These functions determine the width of the jth element in the horizontal direction, and the length of the kth element in the vertical direction, respectively, where $W(=1)$ denotes cavity width and $H(=8)$ cavity height.

Here

$$\hat{h}_1(j) = \frac{1}{\bar{h}_1 (E_x + 1 - 2j)^2 + 2} \quad \text{for } j = 1, \ldots, E_x$$

and

$$\hat{h}_2(k) = \frac{1}{\bar{h}_2 |E_y + 1 - 2k| + 2} \quad \text{for } k = 1, \ldots, E_y$$

control the element width and length distributions, respectively, for given E_x, E_y, where

$$\bar{h}_1 := W/E_x, \quad \bar{h}_2 := H/E_y$$

are the average element width and average element height, in turn.

In Figure 1(a), a graded grid of medium refinement is displayed, revealing, in particular, the relative fineness at the walls; this is shown in greater detail for the south-west corner of

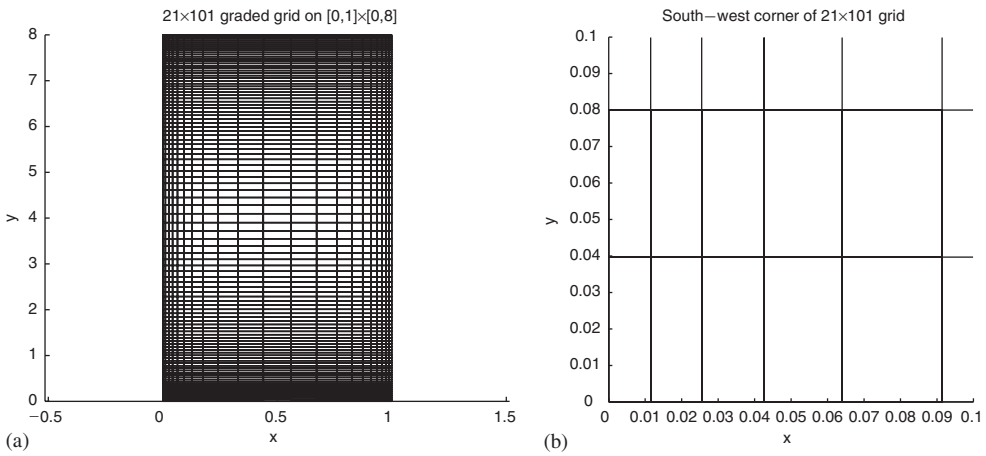

Figure 1. Graded grid of a medium level of refinement: (a) the whole domain and (b) a close-up of the south–west corner.

the cavity in Figure 1(b) where the minimal element size is 0.012×0.04. This region of the cavity, together with its north–east counterpart (due to skew symmetry), was found to be the most sensitive location in general, as regards rapid physical flow changes within the cavity. This is not least due to the strong thermal boundary layers occurring there; indeed, we based our verification that the grids were sufficiently graded near the walls, on whether or not the temperature profile was sufficiently 'smooth' near the horizontal and vertical walls. All three grid types (coarse, medium and fine) were adjudged to pass this 'test' for the given grid functions. Furthermore, with simple real analysis it can be shown that *near the horizontal and vertical walls*

$$h_1 \sim \left(\frac{2\sqrt{2W}}{\pi}\right) E_x^{-3/2}, \quad h_2 \sim \left(\frac{H^2}{(H+2)\log(1+H/2)}\right) E_y^{-1}$$

as $E_x \to \infty$, $E_y \to \infty$, respectively.

RESULTS

Computational results were obtained for each of the three grid types, and for both types of energy solver—hence, a total of six cases. Based on the time history of the flow solution at various 'points' in the cavity (see Reference [1]), the computations reveal an initial 'active' transient state lasting approximately 500 non-dimensional time units preceding a single-frequency periodic state, as illustrated, for example, by Figure 2. Here the temperature and velocity components in point 1, and the pressure difference between points 1 and 4 are shown. These same flow quantities are then depicted over a number of periods in Figure 3.

Three different forms of data were required for the benchmark test, the first of these being 'point data', based on the measurement of flow quantities at the given points in the cavity. The measurement here is based on the average, amplitude (peak-to-valley) and the period of

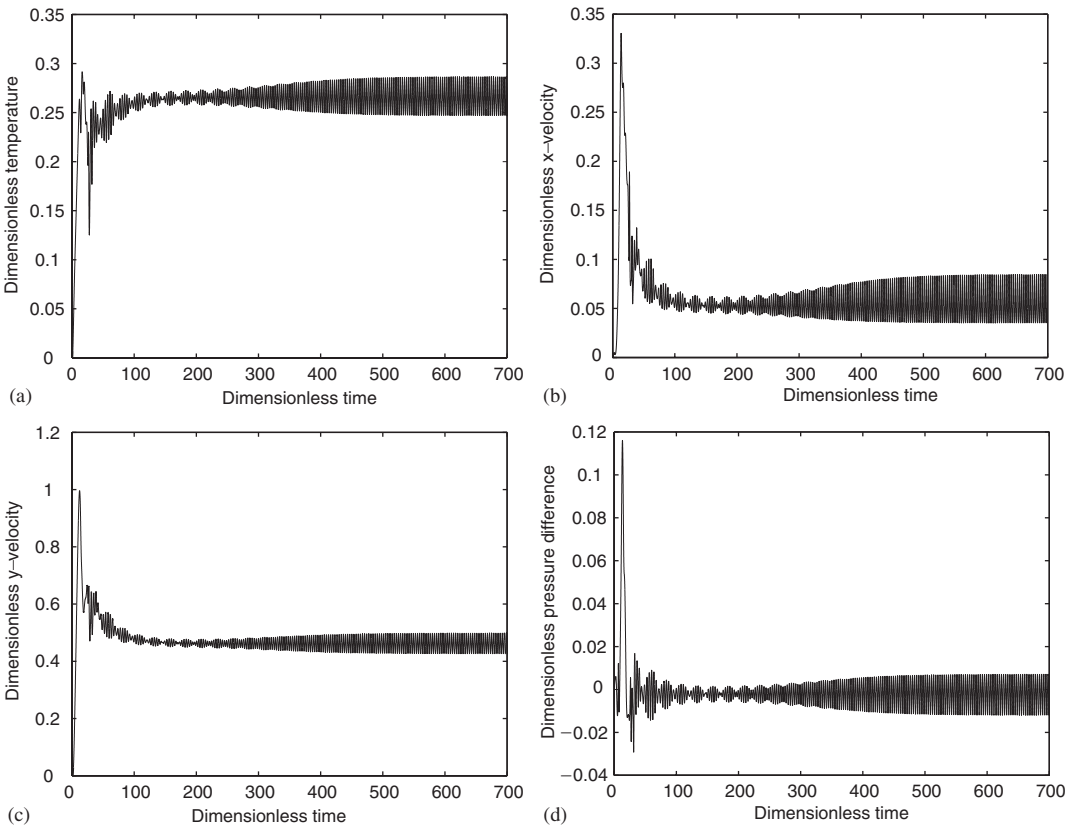

Figure 2. Time histories of dimensionless flow quantities: (a) temperature in point 1; (b) X-velocity component in point 1; (c) Y-velocity component in point 1 and (d) pressure difference between points 1 and 4.

the flow quantity under scrutiny. Before recording measurements, however, the period and amplitude per cycle were first checked for consistency over ten cycles, to ensure that the flow was truly periodic. To calculate the average of the flow quantity, we used Matlab's internal function. Tables I and II show point data for the energy-equation solvers BE and CN. An immediate observation from the tables is that both solvers fail to produce oscillatory motion for the coarse grid case—this is wholly consistent with one of the widely believed disadvantages of working with the Taylor–Hood $Q_2 - Q_1$ element, i.e. its apparent inaccuracy on coarse grids (see e.g. Reference [5, pp. 750–767] for a comparison of accuracy between various quadrilateral (and triangular) finite elements). The averages of the flow quantities can be seen to be most consistent, while the amplitudes are the least consistent; there is also a discrepancy between the values for the amplitudes obtained for the BE and CN cases—our belief, however (given the theoretical knowledge on the types of solver) is that this is principally due to the numerical damping effects present in the former case, and therefore we put more faith in our calculated amplitudes for CN (which theoretically has no numerical dissipative

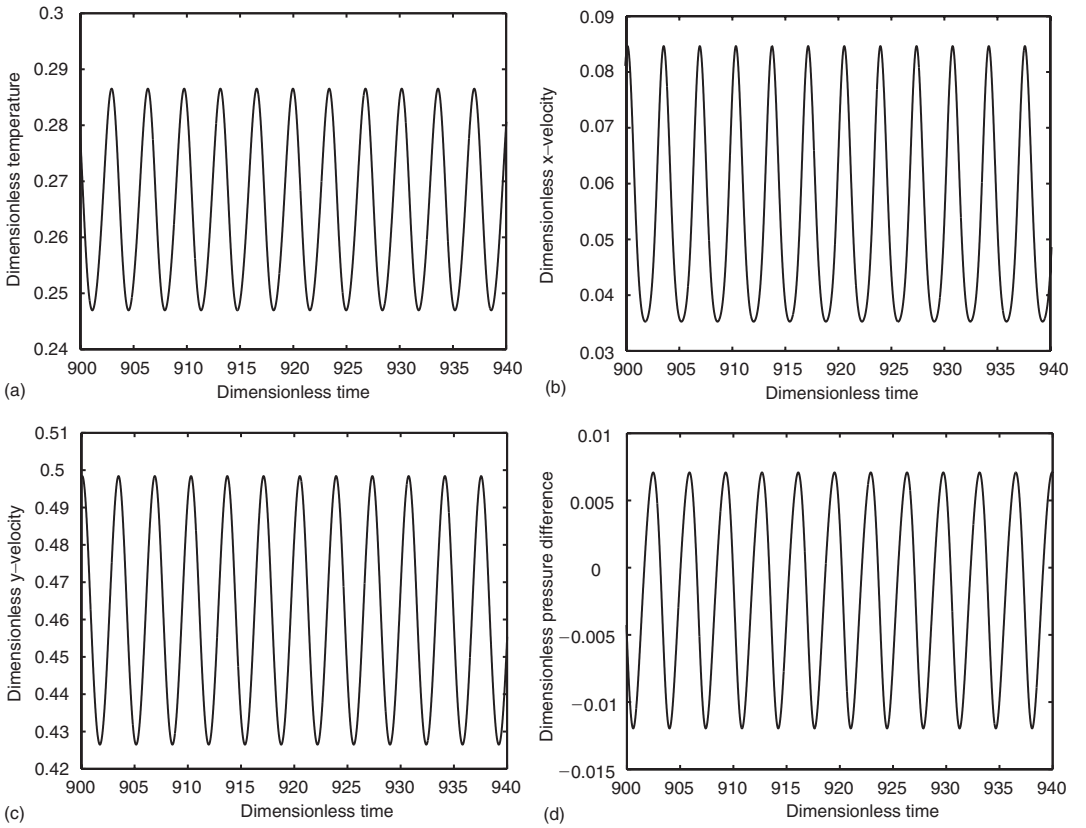

Figure 3. Oscillatory behaviour of flow quantities during periodic phase: (a) temperature in point 1; (b) X-velocity component in point 1; (c) Y-velocity component in point 1 and (d) pressure difference between points 1 and 4.

effects)—this was later confirmed by the accepted 'true' numerical values from Reference [6]. Other noticeable features include the negligible skewness (defined as the average of the temperature values at points 1 and 2) found in all cases, and implying the expected skew-symmetric nature of the perturbation. Finally, we can see that the calculated period differs only slightly from the medium grid to the fine grid; our 'best' prediction of this was 3.412, (based on the fine grid of CN), and this turned out to have a deviation of just 0.015% from the 'true' solution of Reference [6].

Next, 'wall data' values were recorded, specifically, the Nusselt numbers on the vertical walls. We firstly note than the skew symmetry of the flow perturbation should ensure that the values are identical on each wall—this proved to be the case. Figure 4 shows the time history of the Nusselt number on either vertical wall, and reveals very strong initial wall gradients becoming heavily damped before the periodic phase is reached. This again underlines the need for careful grading on the walls, especially during the initial stages of the transient phase. Table III shows the Nusselt values for the CN solver, and for the non-stationary

Table I. Point data computed using the BE solver.

	Grid resolution: 11×51 Time duration: N/A Steps per period: N/A			Grid resolution: 21×101 Time duration: 50 Steps per period: 344			Grid resolution: 41×201 Time duration: 50 Steps per period: 344		
Quantity	Ave	Amp	Per	Ave	Amp	Per	Ave	Amp	Per
X-velocity	0.055	S	S	0.058	0.046	3.44	0.056	0.046	3.44
Y-velocity	0.463	T	T	0.461	0.068	3.44	0.462	0.068	3.44
Temperature	0.264	E	A	0.266	0.036	3.44	0.266	0.036	3.44
Skewness	0	A	T	0	—	—	0	—	—
ΔP_{14}	−0.001	D	E	−0.002	0.018	3.44	−0.002	0.018	3.44
ΔP_{51}	−0.528	Y		−0.534	0.020	3.44	−0.535	0.020	3.44
ΔP_{35}	0.529			0.536	0.008	3.43	0.537	0.008	3.44

Table II. Point data computed using the CN solver.

	Grid resolution: 11×51 Time duration: N/A Steps per period: N/A			Grid resolution: 21×101 Time duration: 50 Steps per period: 341			Grid resolution: 41×201 Time duration: 50 Steps per period: 341		
Quantity	Ave	Amp	Per	Ave	Amp	Per	Ave	Amp	Per
X-velocity	0.0551	S	S	0.0552	0.0494	3.408	0.0563	0.0542	3.412
Y-velocity	0.4632	T	T	0.4613	0.0720	3.407	0.4617	0.0764	3.413
Temperature	0.2641	E	A	0.2655	0.0396	3.407	0.2655	0.0422	3.412
Skewness	0	A	T	0	—	—	0	—	—
ΔP_{14}	−0.0014	D	E	−0.0021	0.0192	3.407	−0.0018	0.0202	3.412
ΔP_{51}	−0.5279	Y		−0.5343	0.0212	3.409	−0.5347	0.0222	3.413
ΔP_{35}	0.5293			0.5362	0.0092	3.407	0.5366	0.0100	3.412

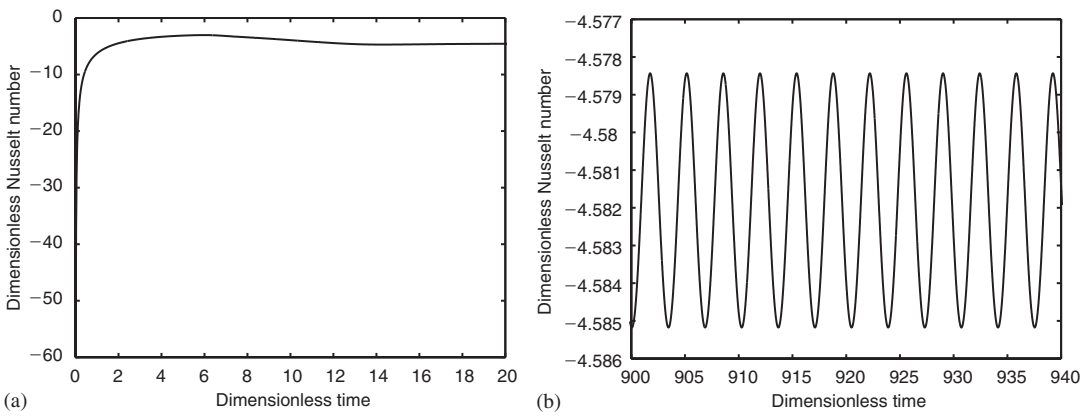

Figure 4. Time history of the Nusselt number on vertical walls: (a) global profile and (b) local oscillatory behaviour during periodic phase.

Table III. Wall data computed using the CN solver.

	Grid resolution: 11×51 Time duration: N/A Steps per period: N/A			Grid resolution: 21×101 Time duration: 50 Steps per period: 341			Grid resolution: 41×201 Time duration: 50 Steps per period: 341		
Quantity	Ave	Amp	Per	Ave	Amp	Per	Ave	Amp	Per
$Nu\ (x=0)$	−4.6217	ST.	ST.	−4.5819	0.0068	3.408	−4.5796	0.0070	3.412
$Nu\ (x=W)$	−4.6217	STATE	STATE	−4.5819	0.0068	3.408	−4.5796	0.0070	3.412

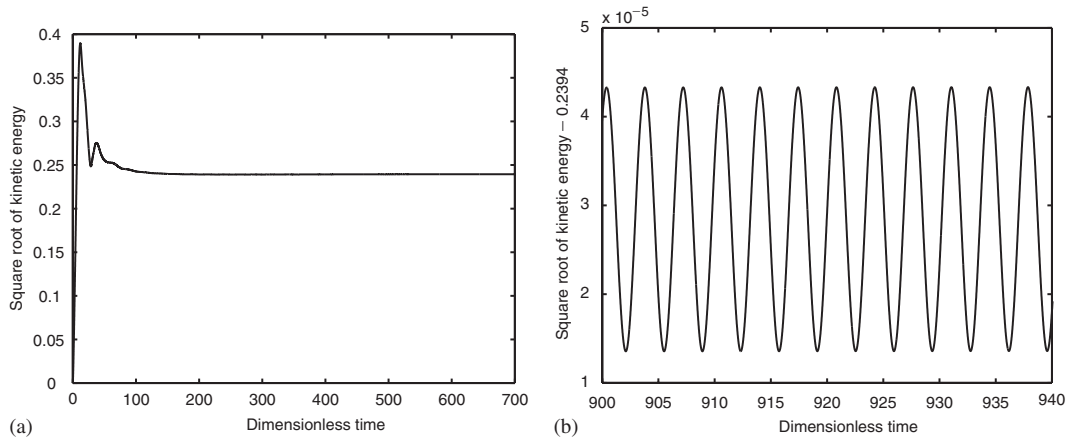

Figure 5. Time history of the velocity metric ($=\sqrt{KE}$): (a) global profile and (b) local oscillatory behaviour during periodic phase (zeroed on 0.2394).

cases (medium and fine grids) we see that the average has a value around −4.58, while the amplitude is relatively small at $O(10^{-2})$.

Finally, 'global data' in the form of a velocity metric, defined as the square root of the kinetic energy (KE) was computed. Figure 5(a) shows the time history of the velocity metric from a global perspective, and it can be seen that this quantity appears to approach steady state, as the periodic phase is approached. In fact, closer inspection (Figure 5(b)) reveals that the velocity metric undergoes small periodic oscillations during this phase. This behaviour is attributable to a weak viscous dissipation ($\sim(Pr/Ra)^{1/2}$) of the rate of change of KE, as can be verified directly by taking the $L^2(\Omega)$ inner product of the momentum terms and the velocity and implementing the incompressibility condition and the homogeneous velocity boundary conditions. In Table IV the specific velocity metric values are tabulated and they indicate that a characteristic value for the speed of fluid is about 0.240.

Table IV. Global data computed using the CN solver.

	Grid resolution: 11×51 Time duration: N/A Steps per period: N/A			Grid resolution: 21×101 Time duration: 50 Steps per period: 341			Grid resolution: 41×201 Time duration: 50 Steps per period: 341		
Quantity	Ave	Amp	Per	Ave	Amp	Per	Ave	Amp	Per
$\hat{u}\ (=\sqrt{KE})$	0.2400	ST.	STATE	0.2394	2.98×10^{-5}	3.407	0.2395	3.30×10^{-5}	3.412

COMPUTATIONAL RESOURCES

The computations were performed on a Compaq XP1000 (single-processor) machine with a clock rate of 500 MHz, total memory of 256 Mb, a peak flop of 500MFLOPs and a Specfp95 rating of 53.9. The CPU/grid point/time step was measured to be approximately 490 μs/pt./step, while approximately 4 Kb of memory per grid point was required.

CONCLUSIONS

The computational results (as reflected, to a degree, in Tables I and II) suggest that the amplitudes of the flow quantities are the most sensitive to time step size and grid resolution, compared to the averages and the periods. Despite this however, a time step size of 0.01 on the finest grid (41×201 elements) proved to be sufficient in obtaining a (time step- and grid-) converged and accurate solution.

In general, the CN solver performed better (regarding accuracy) than the BE solver (and at no extra cost in terms of computing time), and in view of the earlier comments on numerical damping with advection-dominated problems, this is perhaps no surprise. However, both solvers failed to yield a periodic solution after the transient phase on the coarsest grid (11×51 elements), although this is believed to be attributable to the (widely accepted) intrinsic inaccuracy of the $Q_2 - Q_1$ finite element on 'too-coarse' grids. (By comparison, the elements $Q_1 - Q_0$ (bi-linear velocity and temperature, piecewise-constant pressure) and $Q_2 - Q_{-1}$ (biquadratic velocity and temperature, piecewise-bi-linear pressure) were reported to yield periodic solutions on a grid of comparable coarseness to our 'coarse' version [7], although it should also be noted that these elements fail the inf–sup stability condition. The accuracy of the $Q_2 - Q_1$ element on sufficiently fine grids was also reported by another benchmark contributor [8].)

Finally, we remark that we obtained virtually zero skewness in our calculations, a feature consistent with the skew-symmetric nature of the instability mode [1].

REFERENCES

1. Christon MA, Gresho PM, Sutton SB. Computational predictability of natural convection flows in enclosures. *International Journal for Numerical Methods in Fluids* 2002; **40**:953–980.
2. Bristeau MO, Glowinski R, Periaux J. Numerical methods for the Navier–Stokes equations, applications to the simulation of compressible and incompressible viscous flows. *Computer Physics Report* 1987; **6**:73–188.
3. Bänsch E. Simulation of instationary, incompressible flows. *Acta Mathematica Universitatis Comenianae* 1998; **LXVII**:101–114.

4. Saad Y, Schultz MH. GMRES: A generalised minimal residual algorithm for solving nonsymmetric linear systems. *SIAM Journal on Scientific and Statistical Computing* 1986; **7**(3):856–869.
5. Gresho PM, Sani RL. *Incompressible Flow and the Finite Element Method. Vol. 2: Isothermal Laminar Flow.* Wiley: Chichester, 2000.
6. Xin S, Le Quéré P. An extended Chebyshev pseudo-spectral contribution to the CPNCFE benchmark. In *Computational Fluid and Solid Mechanics*, Bathe KJ (ed.), Boston, MA, June 12–15, 2001. Elsevier: Amsterdam, 2001; 1509–1513.
7. Gresho PM, Sutton SB. 8:1 thermal cavity problem. In *Computational Fluid and Solid Mechanics*, Bathe KJ (ed.), Boston, MA, June 12–15, 2001. Elsevier: Amsterdam, 2001; 1482–1485.
8. Westerberg KW. Thermally driven flow in a cavity using the Galerkin finite element method. In *Computational Fluid and Solid Mechanics*, Bathe KJ (ed.), Boston, MA, June 12–15, 2001. Elsevier: Amsterdam, 2001; 1505–1508.

